Establishing Fluid Dynamics Scales Critical to Dynamic Interface Applications and their Impact on Handling Qualities

Quarterly Status Report 7

Period of Performance: 9/5/2022 – 12/4/2022

Prepared by:

G. R. Whitehouse
Continuum Dynamics, Inc.
34 Lexington Avenue
Ewing, NJ 08618-2302

Prepared for:

David Gonzalez
Office of Naval Research
875 North Randolph
Street
Arlington VA 22203

Under Contract No. N00014-21-C-1044

Glen R. Whitehouse

December 7, 2022

Project Summary

One of the most demanding tasks for naval aviators is landing on a moving flight deck in high sea-states (i.e. the dynamic interface (DI) problem - see Figure 1). This task is made even more difficult by aerodynamic disturbances at the landing spot from the flow around the ship's bow, superstructure and deck edges. This highly unsteady ship airwake can lead to significant pilot workload. Flight simulation has long been recognized as a valuable tool for augmenting engineering development and pilot training in DI operations, however, it is most effective when the underlying simulation model has appropriately characterized the complex aerodynamic interactions between the rotorcraft and ship airwake. Given the complexity of the problem, a fundamental difficulty when assessing the simulation approaches is the quantification of "good enough", both from the standpoint of understanding and predicting the underlying physics and also with regards to trainer fidelity (i.e. can the pilot feel/tell a difference). The premise of the proposed effort is to quantify "good enough" with regards to understanding the fundamental aero-physics of a rotorcraft interacting with an external disturbance field to quantify which length and time scales - such as those present in a ship airwake or in the wake of a an upstream aircraft during formation flight/refueling - directly impact the aircraft's fundamental response and flying qualities (FQ) along with the aeromechanics modeling fidelity required to simulate interactions adequately.

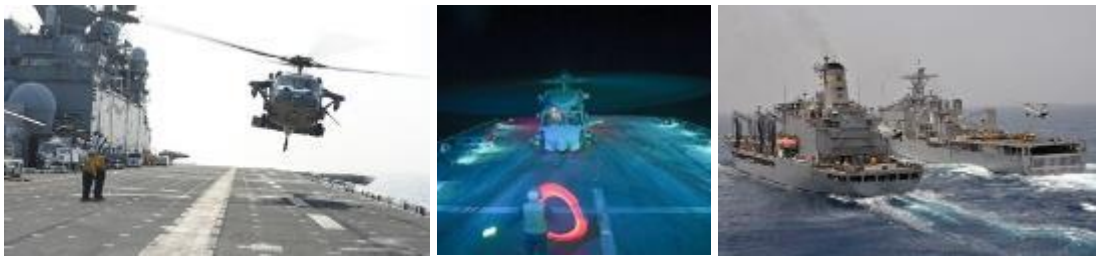

Figure 1: DI scenarios: landing on a moving deck (left), night operations (center) and approaching a pair ships (right)

Several ONR funded efforts that seek to quantify "good enough" have recently completed, or are underway, at the University of Maryland, Georgia Institute of Technology and NAVAIR, where the academic researchers are focusing on understanding the response of a wing to the wake shed by canonical structures [1] and the latter (Generalized Airwake Goodness Evaluation) program seeks to represent the entire DI scenario with a variety of methods. This effort does not seek to duplicate that work, rather to complement it by focusing on several fundamental unknowns in the rotorcraft community, namely:

1. What spatial and temporal scales, present in a disturbance field, matter from Flight Dynamics (FD) and FQ standpoints? Beyond the obvious constraints (i.e. larger than a rotor radius and those that induce velocities larger than the wake induced velocity), how does a rotor respond to different size disturbances and how does the rotor type influence this? For example, in general, a rotor acts to filter the influence of a disturbance field, but the level of filtering will vary significantly between an articulated flexible rotor (H-60) and a gimballed stiff one (V-22). Moreover, rotors typically respond ~90^o out of phase of the disturbance, whereas fixed aerodynamic surfaces response directly in-phase, which results in a fundamentally different response between rotorcraft types (i.e. helicopter vs. tiltrotor).

2. How do these scales vary when the effects on the full aircraft are accounted for? The primary response from the helicopter will be dominated by that of the rotor, though there may still be significant response associated with the disturbance induced flow on the fuselage, empennage and tail rotor.
3. How do these scales vary with aircraft configuration/type (i.e. conventional helicopter vs. tiltrotor)? The primary response from the helicopter will be dominated by that of the rotor, whereas the tiltrotor may respond primarily in a fixed wing manner associated with the induced flow on the wing. Of course, the tiltrotor's response will also vary with nacelle angle, and it is well known that the V-22's response to wake disturbances (i.e. during formation flight) is quite different to other rotorcraft in the Navy's inventory [2].
4. How do these scales vary with aircraft flight condition, and can valid modeling simplifications be made (i.e. distorting vs. classical frozen disturbance field)? Work by Whitehouse and Brown for helicopter rotors [3-7] suggests that for high speed flight, the traditional frozen field (superposition) assumption may be adequate, but that at the low speeds associated with DI operations, a distorting disturbance field and wake are required because the response is critically different.

Developing an understanding of fundamental aircraft aeromechanic response, FD, and FQ to the unknowns outlined above would provide great utility to the community with regards to establishing the level of modeling fidelity required to accurately simulate disturbance interactions, the level of fidelity required to be output by CFD simulation generated ship airwake databases for training scenarios, and the quantification and specification of handling qualities to types of disturbance fields that can be used to define future and ongoing training and aircraft performance requirements and specifications, such as ADS-33 [8].

Technical Objectives

The goal of the effort is to develop a fundamental understanding of the relationship between the length and time scales typically present in disturbance fields experienced by Naval aviators (i.e. ship airwakes, wing wakes etc.) and rotorcraft FD and FQ when the fully-interacting fluid dynamics of the airwake and rotor wake and flight mechanics are accounted for. With this information in hand, the engineering community would be better able to understand the relationship between aircraft type, ride quality, FD and FQ during flight conditions where disturbance fields are encountered. The community would be able to more accurately define trainer requirements, minimum experimental campaign requirements, minimum CFD modeling requirements and consequently establish a benchmark to evaluate CFD predictive capability. Furthermore, the conclusions of this work would also directly impact the development of requirements for new aircraft given the direct correlation between FD and FQ. The proposed effort would undertake the research required to develop such an understanding, with disseminating the observations and conclusions of the work to the Navy and the broader FD, FQ and handling qualities communities - a key objective from the outset. The effort will be structured using a build-up approach that first focuses on defining relevant disturbance fields followed by predicting and understanding the fundamental aeromechanics response (i.e. aerodynamic forces and moments and rotor dynamics). The effort would culminate in predicting the flight dynamics and handling qualities for realistic, but generic, helicopter and tiltrotor configurations that include representations of flight controls, propulsion system and cross-

coupling characteristics. The key objectives for the effort roughly form the main tasks and are as follows:

1. Define the spatial and temporal fluid dynamic scales present in relevant disturbance fields and develop numerical representations for testing (Year 1).
2. 6-DOF generic model assembly and shakedown testing to ensure correct operation and functionality.(Year 1)
3. Define aeromechanics performance and HQ metrics along with a detailed simulation test matrix that includes systematic and consistent model fidelity build-up (Year 1-2).
4. Undertake simulation of a generic helicopter interacting with frozen and distorting disturbance fields to establish fundamental response characteristics (Year 2).
5. Undertake simulation of a generic tiltrotor interacting with frozen and distorting disturbance fields to establish fundamental response characteristics (Year 2).
6. Develop a realistic full helicopter model and undertake simulations of interactions with frozen and distorting disturbance fields to establish flight dynamics and handling qualities response (Year 3).
7. Develop a realistic full tiltrotor model and undertake simulations of interactions with frozen and distorting disturbance fields to establish flight dynamics and handling qualities response (Year 3).
8. Documentation and dissemination of observations and conclusions to the Navy and the wider FD/HQ community (Years 1-3).

Summary of Work Conducted During Reporting Period

During this progress period, work has continued on the development and testing of the method for formulating canonical airwake presented in the previous progress report. In addition, CDI has worked on re-integrating its CHARM software with the Example Helicopter (H-60 like) model provided with the Navy's CASTLE simulation environment.

CASTLE Simulation Model Rehost

Work has been initiated during this reporting period on re-hosting NAVAIR Manned Flight Simulator (MFS) simulation models at CDI to support airwake modeling and its effect on dynamic interface virtual simulation. For this effort, two airframe models will be used: the MFS "ExampleHelo" model and the V-22 simulation. The ExampleHelo model is a generic model of the H-60 based on publicly-available source data (i.e. [9] amongst others) that is distributed by MFS for advanced aerodynamic model integration studies, among other applications. The simulation model was provided by MFS to CDI in support of this effort and subsequently has been re-hosted at CDI (i.e., source code built and test cases executed). Representative results illustrating the pedal response in hover are shown in Figure 2.

An important aspect of the current effort is to examine aerodynamic modeling fidelity requirements for predicting rotorcraft handling qualities and dynamic response characteristics during shipboard operations (i.e., due to ship airwake disturbances). A core component of this investigation is use of physics-based models, including free wake (vorticity-based) models for the rotor wake and rotorcraft-airwake interactions. This investigation will be supported by integration of the CDI CHARM Module with the airframe rotor model. In previous work, CDI has coupled a variant of the CHARM module (denoted CharmSI for CHARM with Shipboard

Interactions) with the MFS "FVMS Models" library, which is a generic flight dynamics modeling library for supporting rotorcraft simulation model build-up. In this case, CHARM provides an alternative inflow model to more conventional (dynamic inflow / finite-state inflow) models, which may be enabled in a given airframe simulation through the CASTLE user interface. This framework has been used in previous pilot evaluation of advanced aerodynamic models within a Navy fleet trainer (see Figure 3 and [10]).

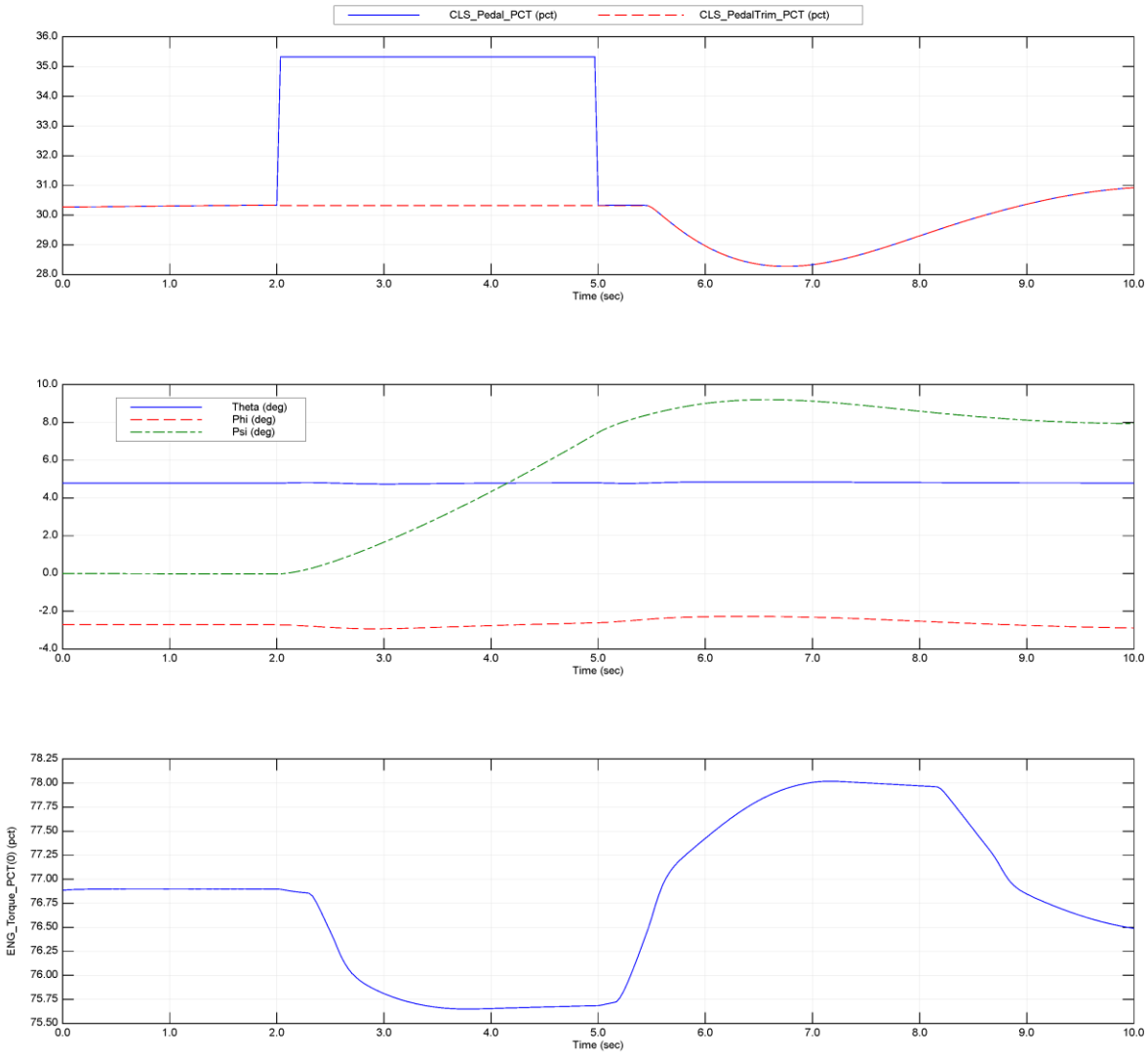

Figure 2: ExampleHelo Simulation Time Histories for Hover Check Case

A primary focus of the current effort has been to update the FVMS rotor-CHARM interface since both the FVMS Models library and CHARM interface have evolved since the H-60 pilot evaluation performed in 2016 and described in [10]. In parallel to this effort, CDI has updated the FVMS-CHARM interface to support a pilot evaluation for the MFS V-22 simulation (to be conducted in December 2022). This simulation model, which will be applied in the present effort, required updating the CHARM interface for use in FVMS Models version 2020.1. Some additional development is required for use with the ExampleHelo simulation, which is based on

FVMS Models version 2021.1. It is anticipated that these remaining code updates will be completed during the next reporting period, at which point both ExampleHelo (H-60) and V-22 flight dynamics will be available for investigation of airwake scaling behavior on rotorcraft flight dynamics.

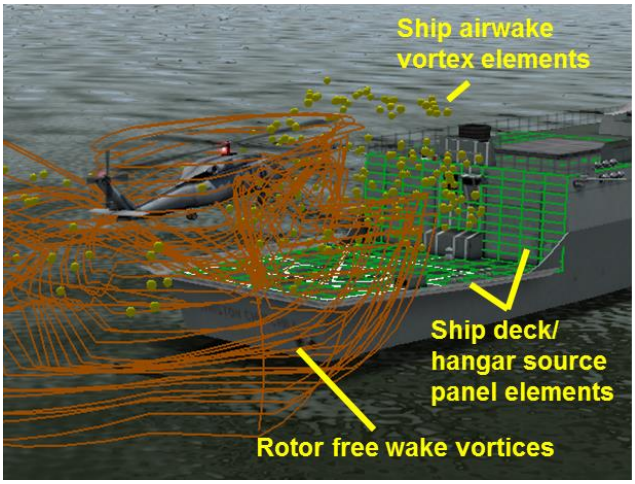

Figure 3: CHARM Model of Rotorcraft Shipboard Operations (from [10])

Simplified Wake Representation

Work during the present reporting period has focused on developing an initial set of nondimensional and potentially scalable parameter relations that provide insights into physical flow phenomena and can be used to reconstruct airwake velocities for arbitrary rectangular configurations. These parameters represent inputs to analytical models that capture time-averaged velocity profiles across various planes. We demonstrated that representative 3D reconstruction of time-averaged velocity fields could be achieved from the planar predictions in the previous progress report. Recent work focused on the physical insights obtained from the parametric model and its potential scalability. Longitudinal velocity profiles associated with flow over the cube will serve as starting point, and the scalability of the resulting parameter relations and associated model will be tested on using different rectangular configurations in the subsequent reporting period.

A description of the CFD simulations is provided next for reference, followed by a description of the analytical model employed for longitudinal velocity fitting. We then examine the variation of model input parameters across three 2D planes, discuss how the variation correlates with physical flow phenomena and present simplified nondimensional and potentially scalable relations that allow us to adequately capture the time-averaged velocity profiles.

CFD Simulation

Development of canonical airwake models has centered on flow simulation over a simple cube. The primary flow features associated with a headwind flow over a cube are illustrated in Figure 4 and include

- A horseshoe vortex that forms upstream of the obstacle where the flow stagnates and wraps around the cube (feature “A” on the figure);
- On the top and side surfaces, local separation and reattachment regions (“B” and “C” on the figure);

- In the lee of the obstacle, an arch vortex (feature "D" on the figure) that forms due to the separation of the shear layers from the top and side surfaces. The streamlines aft of the obstacle indicate a recirculation region, where the direction of the flow reverses.

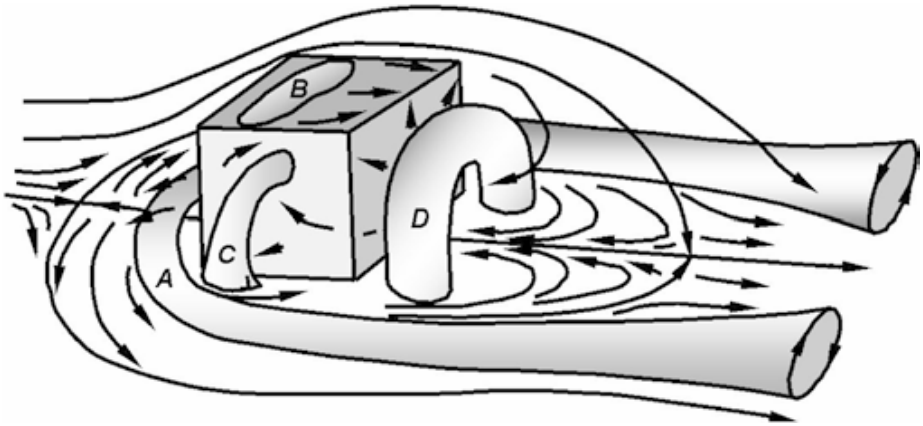

Figure 4: Schematic of principal flow features around surface-mounted obstacle [11].

To generate source data for canonical model development, CFD simulations were performed for a 30 m/s headwind over a 10 m cube using the CDI CGE/VorTran-M flow solver in a manner described in [12] and [13]. Although this speed is larger than would be typically encountered in practice, the use a larger freestream velocity facilitates good numerical conditioning of the compressible flow solver and eliminates the need to use low-Mach number preconditioners in CGE. Moreover, using the higher velocity should not result in any misrepresentation of the primary flow features as the flow field is dominated by separation from the sharp edges, which has a weak dependence on viscosity.

CGE/VorTran-M simulations were performed using a fixed time step of 0.005s, where the transient calculations were preceded by a short steady CGE only simulation to washout flow features associated with impulsively starting the simulation. This sequence enables an expedient solution that does not require the code to resolve and propagate the starting vortices far downstream, as would otherwise be expected from an impulsive start. The transient simulation was then carried out for a duration of 25s, where there first three seconds were used for transition from steady to transient simulation and the subsequent 22 seconds worth of data were recorded for post-processing in 0.1s increments.

Vortex shedding frequency is characterized by the Strouhal number, which is defined as

$$St = \frac{fb}{U} \tag{1}$$

where f is the vortex shedding frequency and b is the characteristic length. Results from literature indicate dominant periodicity for flow aft of a cube at a distance of 6H [14] to have a characteristic frequency of $St = 0.104$ [14, 15], where H is the cube height. Using 10 m cube length as characteristic length and the freestream velocity of 30 m/s as characteristic velocity, this Strouhal number corresponds to a vortex shedding frequency $f = 0.3$ Hz, which, in turn, corresponds to a period of 3.2 seconds. The trimmed 22 second simulation duration thus allows for approximately 7 cycles of vortex shedding to be captured. CFD results were compared to results from literature in previous progress reports.

Figure 5 illustrates that the CFD predicts the flow features described previously, and our approach to formulating canonical airwake models for arbitrary ship configurations begins with

fitting 2D analytical models onto the velocity profiles noted along these three reference planes shown in the figure. Two-dimensional models were chosen as starting point for simplicity and because they provide a basis for a fundamental, "ground-up" approach to airwake reconstruction while providing insights into flow phenomena. This approach will be described further in the subsequent sections, but please note that the right-handed coordinate system shown in Figure 5 has its origin at the center of the bottom face of the cube. Freestream is in the negative *z* direction. All position coordinates in this report are defined relative to this coordinate system unless stated otherwise.

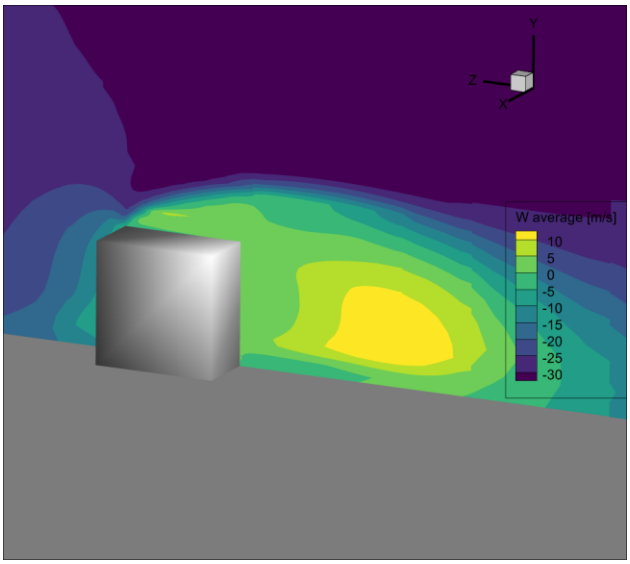

(a) x=0m midplane showing top surface separation and back step recirculation

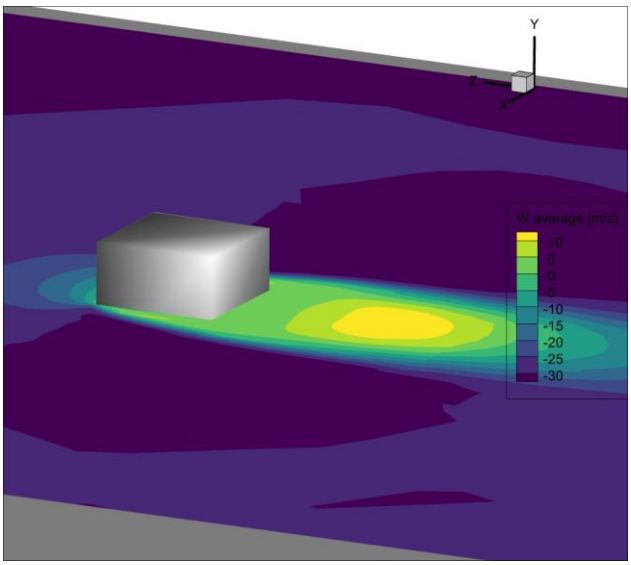

(b) y=5m midplane showing side surface separation and symmetrical aft recirculation

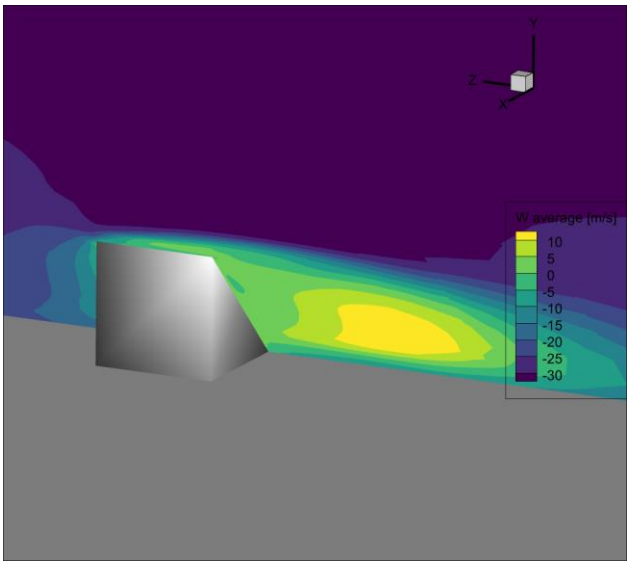

(c) diagonal plane that capture corner edge separation and aft recirculation

Figure 5: Contour of time-averaged longitudinal velocity for a 30m/s headwind simulation over a 10m cube using CGE/VorTran-M along planes containing primary flow features; center of coordinate system is at the center of the bottom face of the cube.

Analytical Model

The vortex model proposed by Banks and Meroney [16, 17] for modeling conical vortices on building roofs was used as basis for the analytical model, and a schematic of the model is shown in Figure 6. Here, a vortex of radius h with center at point O is placed above the surface such that it touches the surface at point S. To allow for a smooth transition from constant vorticity within the vortex to regions of zero vorticity where potential flow theory applies, a transition region is introduced, with point *M* on Figure 6 indicating the start of the potential flow region. Point *C* represents the location of maximum velocity in the transition region and is typically set to the midpoint location in the transition region. The vortex is envisioned to be driven like a wheel, spinning due to freestream velocity acting at point *M* [16]. Banks and Meroney provide piece-wise continuous expressions for velocity across five distinct regions of the domain, shown in Figure 7. The nondimensional coordinate $a = \zeta/h$ will be used when referencing distances relative to the vortex center. The core is assumed to have a diameter of $0.2h$ and represents a region dominated by viscosity, where flow follows a solid body rotation motion. In the region between the core and transition ($0.2 < a < 1$), the velocity profile is based on a power curve fit to the velocity profile obtained from a Navier-Stokes based simulation for a 65° swept delta-wing at a 10° angle of attack at 70% chord and Mach number $M = 0.85$. This relation is used because of the similarity between conical vortices on the roof of a building and delta-wing vortices observed on delta-wing aircraft. Between the core and roof surface (-1 < a < 0.2), pressure changes occur due to centrifugal accelerations of the vortex, such that the resulting governing equation is (see [16]):

$$\frac{dP}{dn} = \frac{\rho U^2}{R_c} \tag{2}$$

where P is the pressure, n is the unit normal to the curvature, ρ is the fluid density, U is the fluid speed in the direction of the vortex, and R_c is the radius of curvature. In the potential flow region, flow merges with freestream and both Bernoulli's equation and Eq. (2) are obeyed. The equations representing the velocity profile from this model are summarized in Table 1. There are three primary inputs to the model:

1. vortex radius (h),
2. location of point M (R_M), and
3. velocity at point M (U_M).

Sample results for the longitudinal velocity at two locations on the top of the surface along the midplane shown in Figure 5(a) are shown in Figure 8, where the model adequately captures the velocity profiles predicted by CGE/VorTran-M.

Table 1: Velocity profile equations for Banks and Meroney vortex model [16]; $\boldsymbol{a_1 = 0.2}$ is used to delimit vortex core size, $\boldsymbol{a_2 = 1}$ is used to delimit vortex size, $\boldsymbol{a_3}$ is used to demark start of potential flow region, $\boldsymbol{a_{max}}$ is used to denoted the point in the transition region where maximum velocity is obtained, $\boldsymbol{U_{max}}$ is taken to be the velocity at point M, $\boldsymbol{U_{a_1} = U_{vortex}(a_1)}$, $\boldsymbol{U_{a_2} = U_{transition}(a_2)}$, $\boldsymbol{U_{a_3} = U_{tranistion}(a_3)}$ and $\boldsymbol{n' = n/h}$.

R_c/h	Range	Description	Velocity Equation
$-\infty$	$a = -1$	Roof surface	$U = 0$
$a/(1+a)$	$-a_2 < a < -a_1$	Between roof and vortex core	$U(a) = -U_{vortex}(a) = -U_{a_2} \cdot \sqrt{a/-a_2}$
a	$\lvert a \rvert < a_1$	Viscous vortex core	$U(a) = U_{core}(a) = U_{a_1} \cdot a/a_1$
$a + a^3/2$	$a_1 < a < a_2$	Vortex, above core	$U(a) = U_{vortex}(a) = U_{a_2} \cdot \sqrt{a/a_2}$
$a + a^3/2$	$a_2 < a < a_3$	Transition region	$U(a) = U_{transition}(a) = \frac{U_{max} \cdot 2 \cdot (a/a_{max})}{1 + (a/a_{max})^2}$
$a + a^3/2$	$a_3 < a$	Potential flow region	$U(a) = U_{potflow}(a) = U_{a_3}\sqrt{e^{\int_{a_3}^{a} \frac{-2}{(R_c/h)} dn'}}$

A modified version of the model was introduced to capture longitudinal velocity profile associated with the separation aft of the obstacle (seen in the contours in Figure 5). The equations in Table 1 were still applied but in this case, the vortex was shifted upwards such that a transition region existed below the vortex center as well, as depicted in Figure 9. With this shift, the vortex model can be thought of as wheel being spun at two points: point M_{upper} at a velocity $U_{M_{upper}}$ and point M_{lower} at a velocity $U_{M_{lower}}$. The vortex core size, which was previously set to $0.2h$, was allowed to vary. Additionally, closer to the ground, the longitudinal velocity was set to a constant ground velocity (U_0), which, in most cases, was set to zero. Since we are using results from an inviscid simulation as truth model, velocity at the ground is not necessarily always zero. Inputs to the modified model consisted of

1. location of vortex center (r_c).
2. vortex radius (h),
3. vortex core radius fraction (c)
4. location of point M_{upper} ($R_{M_{upper}}$),
5. location of point M_{upper} ($R_{M_{lower}}$),
6. velocity at point $R_{M_{upper}}$ ($U_{M_{upper}}$),
7. velocity at point $R_{M_{lower}}$ ($U_{M_{lower}}$),
8. location of point close to ground (r_0) below which the constant velocity was assumed, and
9. velocity near ground (U_0).

Sample results are given in Figure 10 for z=-18m along the mid plane shown in Figure 5(a).

The two versions of the Banks and Meroney model allowed for 1D predictions of longitudinal velocities at specified span (z) locations along the planes shown in Figure 5. The inputs to the models provide basis for parametrization and scaling as will be described in the next section. For 2D predictions across each plane, polynomial functions for the model inputs as a function of span location z were derived using parameters obtained, initially, via manual fitting at multiple span locations. This extension to 2D effectively assumes that an infinite number of overlapping vortices of differing sizes exist in that plane. The manual fitting procedure was overhauled and replaced with automated scripts that determine model fit parameters via optimization during the previous reporting period. Aft of the obstacle, a piece-wise approach was initially adopted, where the vortex was assumed to have an ellipse shape in the vicinity of the obstacle and the infinite vortex model was employed further downstream. The ellipse-based model was dropped in favor of the infinite vortex model approach, which adhered better to the automated parameter fitting scripts that were implemented.

It is important to emphasize here that the even though the model proposed by Banks and Meroney is a vortex model associated with flow physics, we refer to the versions adopted here as "analytical" models as they are primarily used as mathematical constructs that were found to represent CFD source data. Although model input parameters provide insights into physics of flow features, proper physical characterization of these features as vortex phenomena such as point vortices, vortex lines or sheets was not a focus in this work thus far and will be re-examined as necessary.

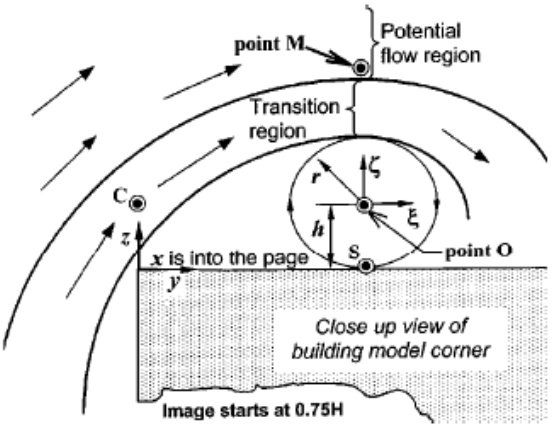

Figure 6: Illustration of the vortex model proposed by Banks and Meroney [16].

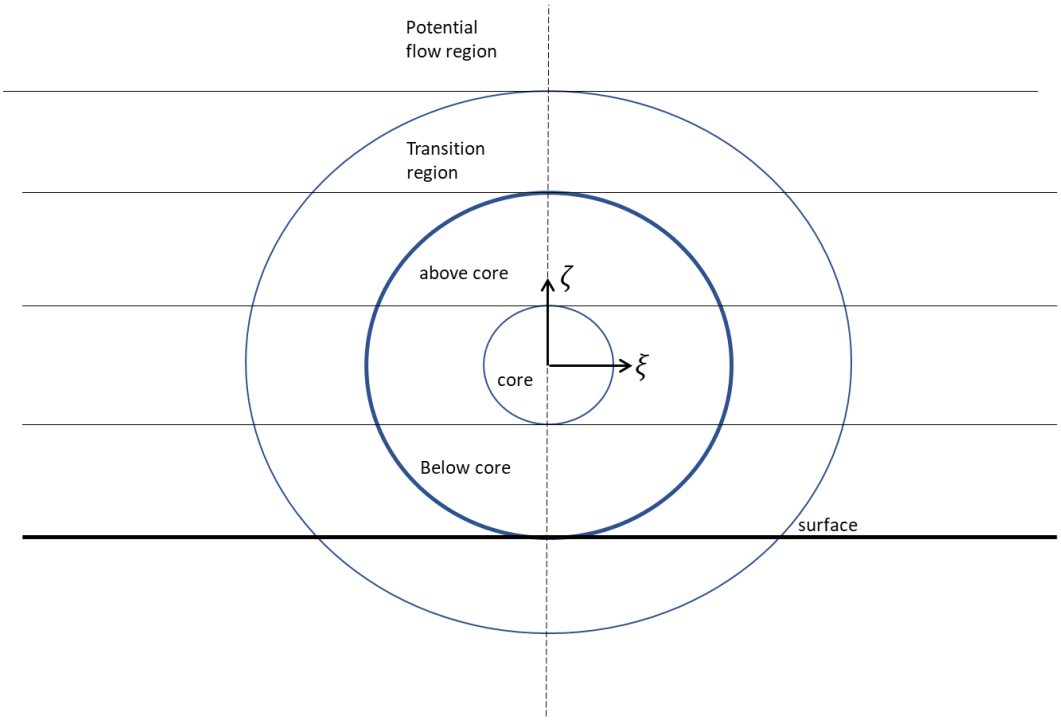

Figure 7: Illustration of the vortex model proposed by Banks and Meroney highlighting the five regions considered.

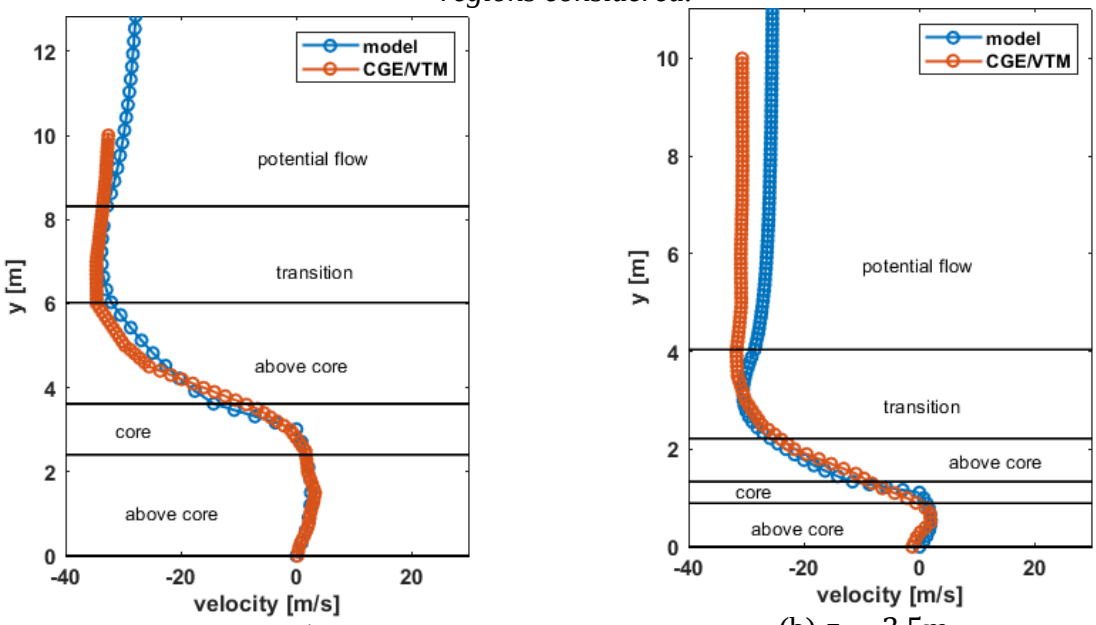

(a) $z = -3.5m$ (b) $z = 3.5$m

Figure 8: Longitudinal velocity profile at two span locations over top surface of cube; height plotted relative to top surface.

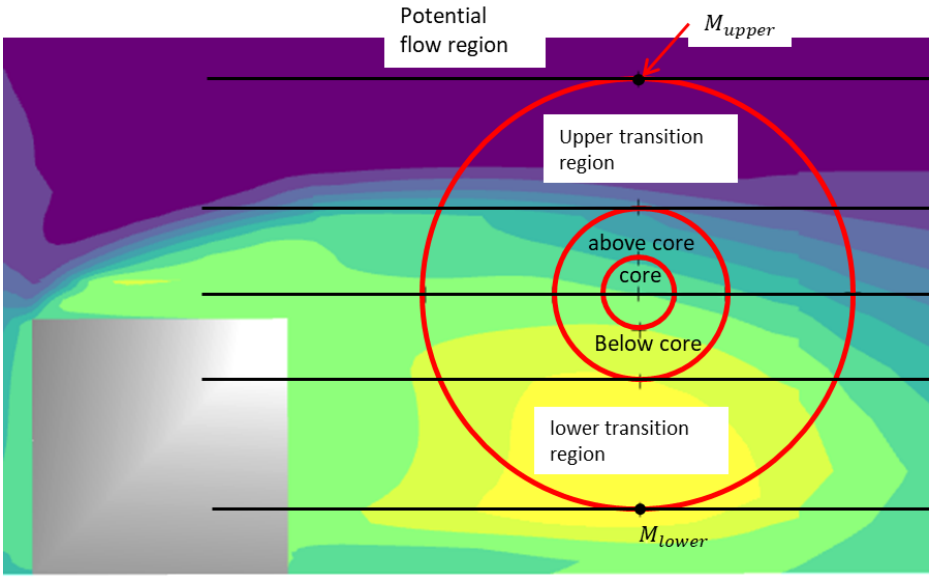

Figure 9: Illustration of modified Banks and Meroney vortex model shifted upwards.

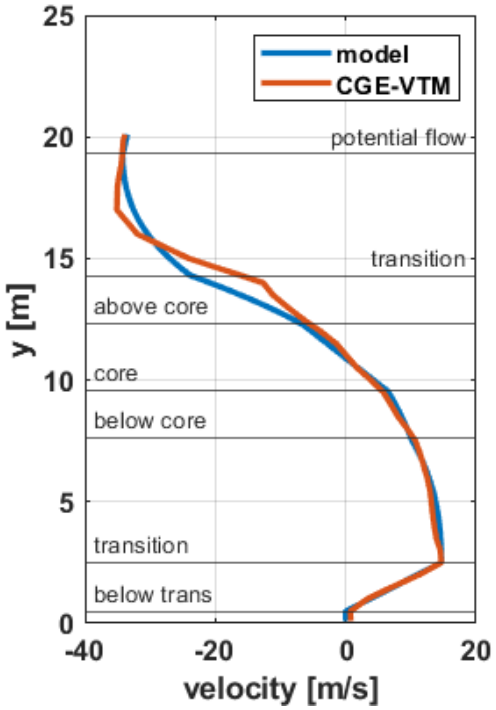

Figure 10: Longitudinal velocity profile along a vertical line through z=-18m in the lee of the cube.

Nondimensionalization and Parametrization

In this section, we examine the spanwise variation of model input parameters along the three planes shown in Figure 5 and provide simplified nondimensional relations that allow us to adequately capture the corresponding longitudinal velocity profiles, whilst simultaneously providing a basis for scalability to other rectangular configurations. These parameters were obtained using the automated parameter fitting scripts described in the previous progress report.

We consider each plane in Figure 5 sequentially. Note that for the descriptions that follow, we restrict our attention to the region *aft* of the obstacle up to $z = -25m$, which corresponds to $2L$ downstream, where $L = 10$m is the cube length. The modified Banks and Meroney model described above applies within this region, and coordinates along the x, y, and z axes are expressed in nondimensional terms using obstacle width (W), height (H) and length (L), respectively.

Midplane x=0W

Model input parameter variation along the midplane shown in Figure 5(a) is shown in Figure 11, where the overbar indicates nondimensional quantities. Distance parameters $r_c, h, R_{M_{upper}}$, $R_{M_{lower}}$ and r_0 were nondimensionalized using the obstacle height H while the velocity parameters $U_{M_{upper}}, U_{M_{lower}}$ and U_0 were nondimensionalized using freestream speed U_∞. The trends exhibited in the parameter variations provide some insights into physical phenomena:

- the vertical location of vortex center $\bar{r}_c$ along the plane reduces as we proceed downstream in a manner similar to the shear layer shed from the top edge of the back face of the cube (see Figure 4);
- the size of the vortex radius $\bar{h}$ increases almost linearly beyond $\bar{z} = 0.4$;
- the size of the vortex core region $\bar{c}$, where flow follows a rigid body rotation model increases linearly from $\bar{z} = 0.4$ to $\bar{z} = 1$, beyond which it starts decreasing;
- the vertical location of the upper spin point $\bar{R}_{M_{upper}}$ (see Figure 9), which demarks the start of potential flow region, remains approximately constant at $1.855H$ when the plotting range in Figure 11 is examined;
- the vertical location of the lower spin point $\bar{R}_{M_{lower}}$, where maximum velocity in the direction opposite of freestream is noted, increases almost linearly;
- flow acceleration due to shear layer shedding is apparent in the trendline for the upper spin velocity $\bar{U}_{M_{upper}}$, which initially has a magnitude of $1.2U_\infty$ immediately aft of the obstacle and progressively reduces to $1U_\infty$ as we proceed downstream;
- the magnitude of the lower spin velocity $\bar{U}_{M_{lower}}$ gives a direct measure of the magnitude of the recirculation velocity as it represents the maximum velocity in the direction *opposite* freestream velocity. In Figure 11, this magnitude can be seen increasing up to approximately $\bar{z} = 1.3L$, where peak velocity is close to $0.5U_\infty$, and beyond which it decreases. The location $\bar{z} = 1.3L$ corresponds to $z = -18m$ when dimensionalized, which is close to the -18.9 m location where the primary vortex core was established to be using Tecplot's vortex core extraction features in previous progress reports.

The parameters $\bar{r}_0$ and $\bar{U}$ are artificial artifacts added for better agreement with the CFD simulations that we employ as truth model.

Using the nondimensional trendlines in Figure 11 as basis, we derived the following simplified polynomial relations for the spanwise variation of model inputs:

$$
\begin{aligned}
&\bar{r}_c(\bar{z}) = -0.14\bar{z}^2 + 0.17\bar{z} + 1.1,\\
&\bar{h}(\bar{z}) = 0.1\bar{z} + 0.35,\\
&\bar{c}(\bar{z}) = -0.16\bar{z}^2 + 0.17\bar{z} + 0.49,\\
&\bar{R}_{M_{upper}}(\bar{z}) = 1.9,\\
&\bar{R}_{M_{lower}}(\bar{z}) = 0.088\bar{z} + 0.15,\\
&\bar{U}_{M_{upper}}(\bar{z}) = 0.069\bar{z}^2 - 0.1\bar{z} - 1.15,\\
&\bar{U}_{M_{lower}}(\bar{z}) = -0.33\bar{z}^2 + 0.86\bar{z} - 0.11,\\
&\bar{r}_0(\bar{z}) = -0.012\bar{z} + 0.086,\\
&\bar{U}_0 = 0.
\end{aligned}
\tag{3}
$$

which can be used with the modified Banks and Meroney model enables adequate representation of the longitudinal velocity profile in the $x = 0W$ plane, as shown in Figure 12.

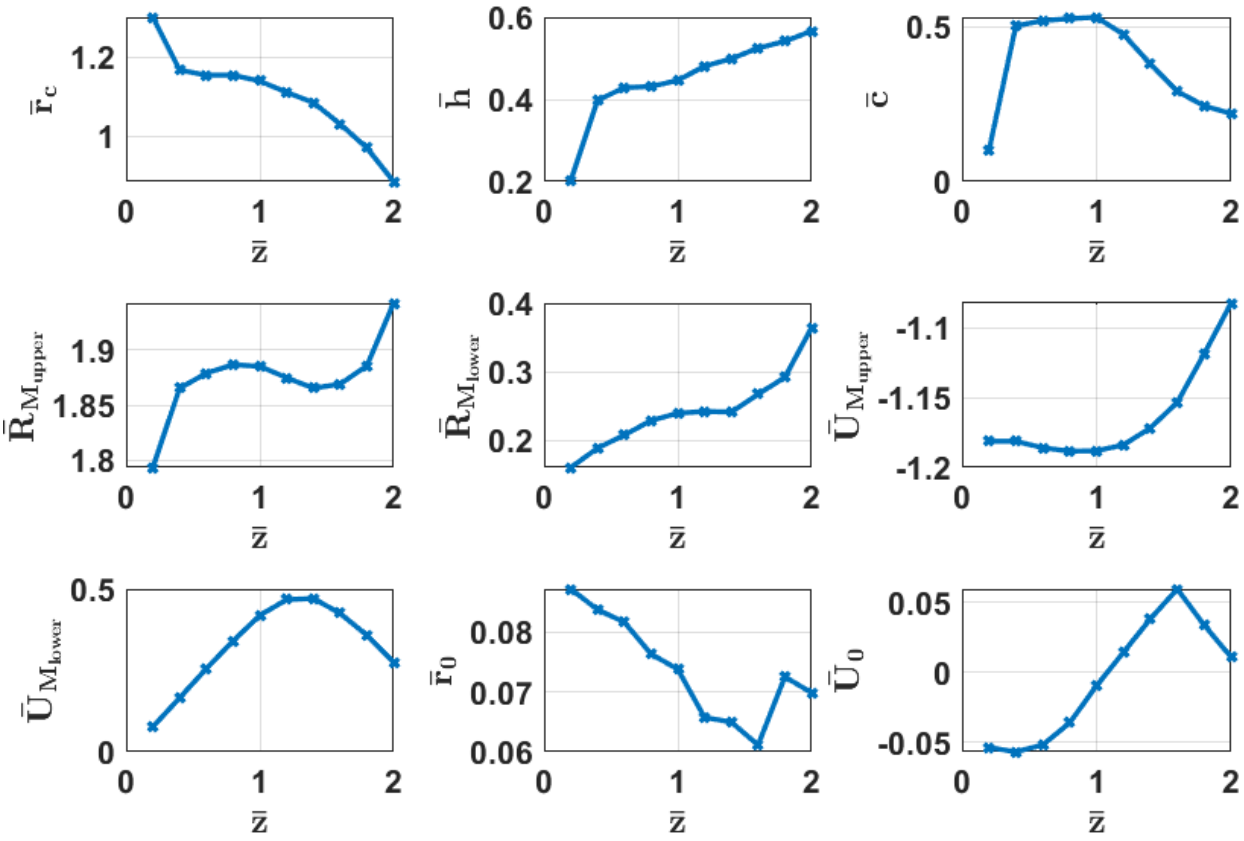

Figure 11: Nondimensional variation of modified Banks and Meroney model input parameters along $x = 0W$ plane; distance parameters nondimensionalized by obstacle height, and span location nondimensionalized using obstacle length such that back face corresponds to $\bar{z} = 0L$.

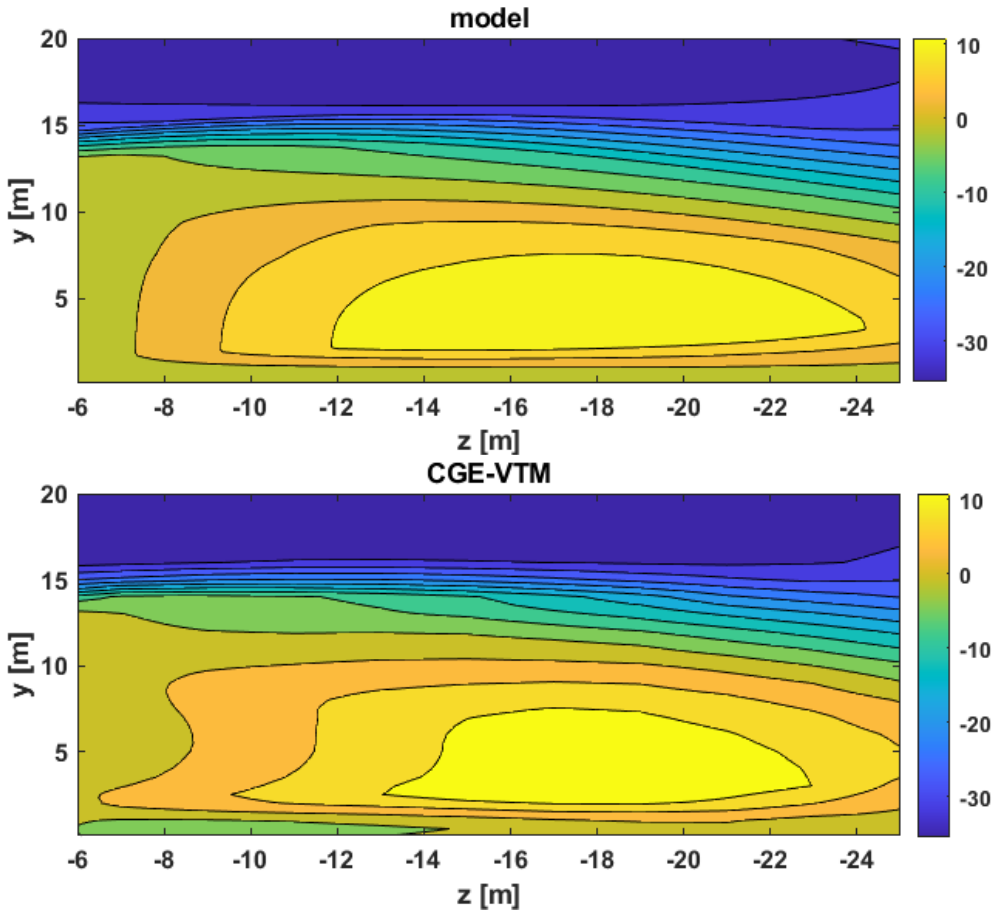

Figure 12: Contour of longitudinal velocity profile across $x = 0W$ plane obtained using model (top) and CGE/VorTran-M (bottom).

Midplane y=0.5H

A symmetric velocity distribution is noted in the $y = 0.5H$ plane in Figure 5(b). Given the resemblance of the profile to the that in $x = 0W$ plane, we conjectured that the simplified parameter relations given in Eq. (3) could be employed here as well. We introduce the $\hat{y}$ axis here to represent the vertical axis employed by the model. In the previous section, $\hat{y}$ coincided with the CGE/VorTran-M y axis and with $\hat{y} = 0H$ corresponding to $y = 0H$, which represents ground. In the current side plane, $\hat{y}$ corresponds to the CGE/VorTran-M x axis. No ground is present but a symmetry condition exists relative to the $x = 0W$ plane. We surmised that using the relations given in Eq. (3) together with the modified Banks and Meroney model with $\hat{y} = 0.5H$ as starting height would be adequate for representing the longitudinal velocity profile for regions $x > 0W$ and $x < 0W$ (symmetry assumed). From the contour plots shown in Figure 13, this hypothesis appears correct. Note that for this plane, the distance parameter relations given in Eq. (3) were dimensionalized using the obstacle *width*, which for a cube equals the height. These equations can also be potentially applied to rectangular configuration where the width does not equal the obstacle height.

The representation employed for the $y = 0.5H$ plane can also be thought of as a 90° counterclockwise rotation of the velocity profile from the $\hat{y} = 0.5H$ location upwards about the $x = 0W, y = 0.5H$ point (see Figure 5(a) and (b)), while appropriately accounting for obstacle

width. The similarity in the velocity profiles also points towards a corresponding similarity that exists between the shear layer (and associated recirculation) from the top and side edges of the back face of the obstacle. Although these coherent features exist as 3D phenomena, they can be analyzed using 2D planar snapshots as we do here.

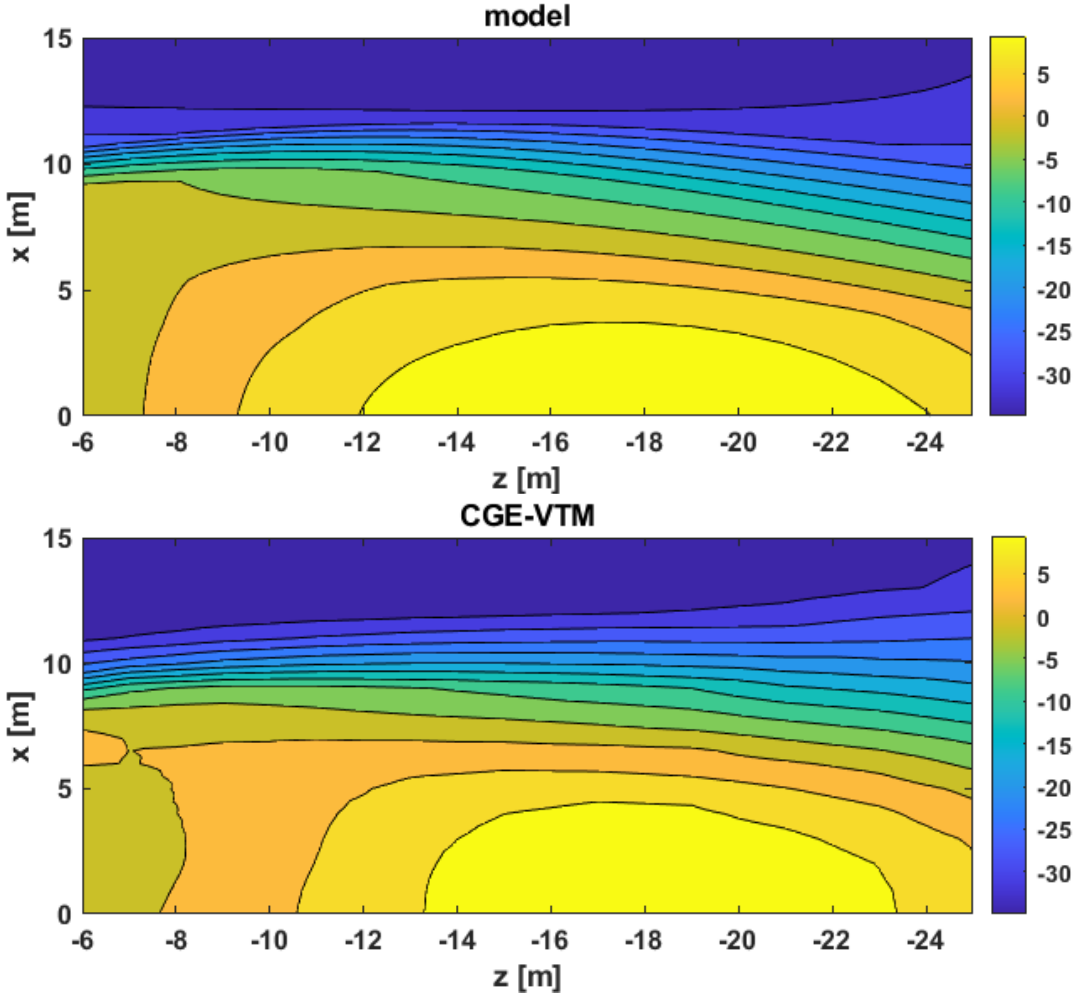

Figure 13: Contour of longitudinal velocity profile across $y = 0.5H$ plane obtained using model (top) and CGE/VorTran-M (bottom).

Diagonal Plane

We now consider the diagonal plane shown in Figure 5(c). As a first attempt, we applied the modified Banks and Meroney model with the relations given in Eq. (3) given the similarity of the velocity profile to that in Figure 5(a). We dimensionalized distance parameters using the diagonal length of L_c =14.14m. The resulting longitudinal velocity profiles are shown in Figure 14. There is a general agreement in the distribution with the CFD predictions, although it is apparent that the model predicts a wider range of positive velocities. Unlike the $x = 0W$ and $y = 0.5H$ planes considered previously, which intersect the middle of the obstacle, the diagonal plane intersects corner edges of the obstacle, which are associated with 3D flow effects. Shear layers shed from the top surfaces interact along that plane, together with deck-edge vortices that result due to pressure differences between the two surfaces.

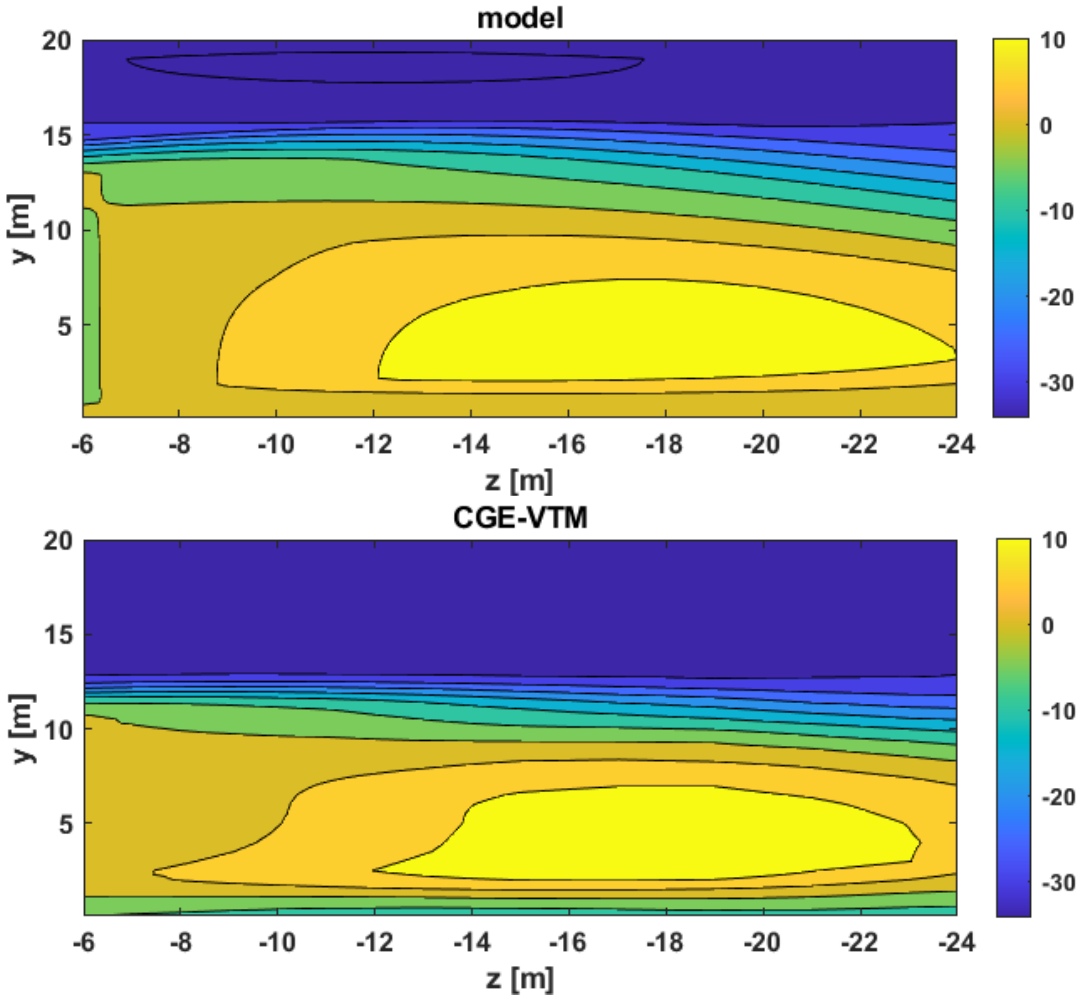

Figure 14: Contour of longitudinal velocity profile across diagonal plane obtained using model with input relations given by Eq. (3) (top) and CGE/VorTran-M (bottom).

Following a similar approach as in the $x = 0W$ plane, we employed the automated parameter fitting scripts to derive optimal parameter values at various span locations along the plane. These are plotted in Figure 15, where distance values have been nondimensionalized using the diagonal length and velocity values using freestream speed.

It is interesting to note the similarity in parameter trends in Figure 15 and Figure 11. With the exception of the vortex radius $\bar{h}$ and the two parameters added for consistency with the inviscid simulation $\bar{r}_0$ and $\bar{U}_0$, similar spanwise variations are noted for the remaining parameters. In fact, the magnitudes and values of the variations of $\bar{R}_{M_{lower}}$, $\bar{U}_{M_{upper}}$and $\bar{U}_{M_{lower}}$in Figure 15 closely match those in Figure 11. The differences seen in the $\bar{r}_c$ and $\bar{R}_{M_{upper}}$ parameter variations can potentially be attributed to the combined effect of the interacting top and side shear layers. The nondimensional range of $\bar{r}_c$ in Figure 11 of $[0.9,1.3]H$ is wider than the $[0.8,1]Lc$ range in the diagonal plane in Figure 15. Physically, this implies the viscous core center is lower in the diagonal plane than in the $x = 0W$ midplane. Similarly, the range of $\bar{R}_{M_{upper}}$ in the $x = 0W$ plane of $[1.8,1.95]H$ is wider than the $[1.52,1.6]Lc$ range across the diagonal plane.

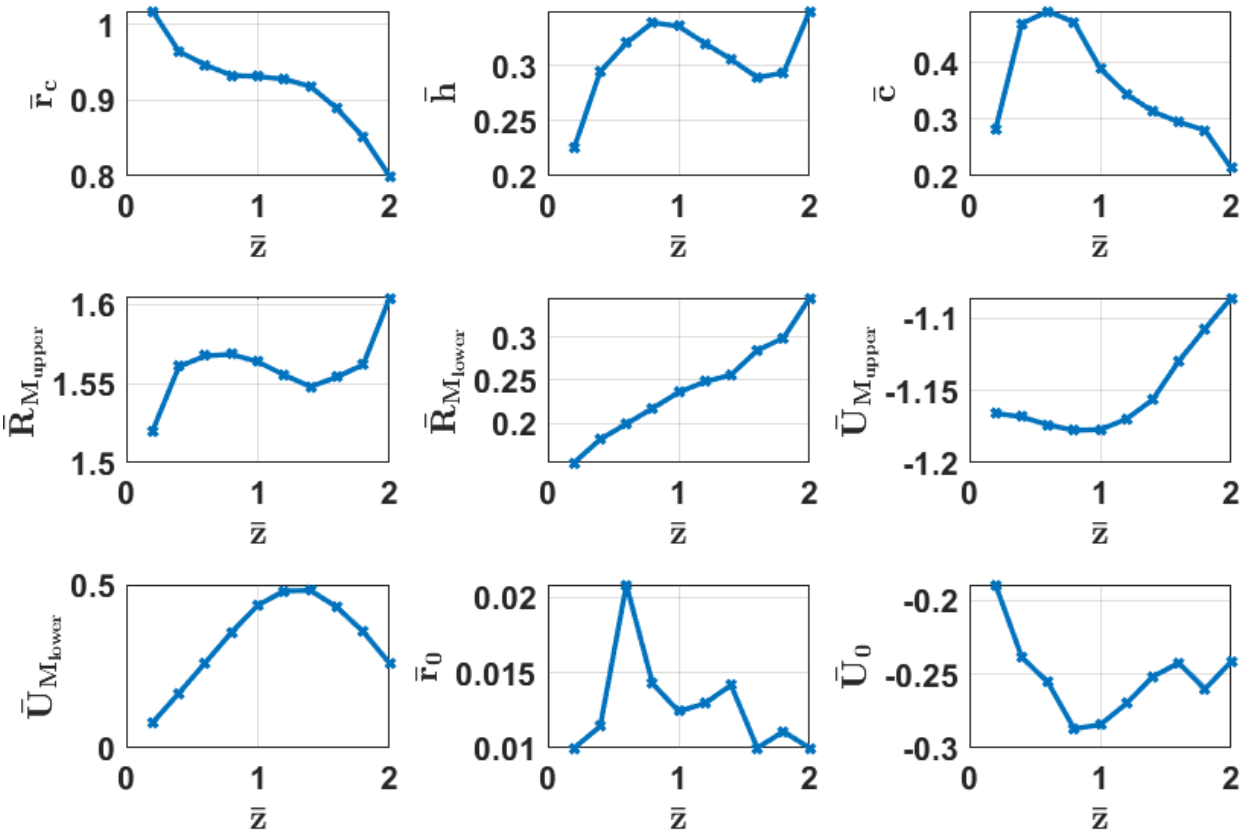

Figure 15: Nondimensional variation of modified Banks and Meroney model parameter inputs along diagonal plane; distance parameters nondimensionalized by diagonal length, and span location nondimensionalized using obstacle length such that back face corresponds to $\bar{z}$ =0L.

We derived the following simplified relations for the parameter variation in the diagonal plane:

$$\begin{aligned}
&\bar{r}_c(\bar{z}) = -0.07\bar{z}^2 + 0.081\bar{z} + 0.93,\\
&\bar{h}(\bar{z}) = 0.024\bar{z} + 0.28,\\
&\bar{c}(\bar{z}) = -0.17\bar{z} + 0.57,\\
&\bar{R}_{M_{upper}}(\bar{z}) = 1.56,\\
&\bar{R}_{M_{lower}}(\bar{z}) = 0.094\bar{z} + 0.14,\\
&\bar{U}_{M_{upper}}(\bar{z}) = 0.06\bar{z}^2 - 0.088\bar{z} - 1.15,\\
&\bar{U}_{M_{lower}}(\bar{z}) = -0.36\bar{z}^2 + 0.92\bar{z} - 0.13,\\
&\bar{r}_0(\bar{z}) = -0.0017\bar{z} + 0.015,\\
&\bar{U}_0 = -0.25.
\end{aligned} \tag{4}$$

Note how closely the equations for $\bar{c}$, $\bar{R}_{M_{lower}}$, $\bar{U}_{M_{upper}}$and $\bar{U}_{M_{lower}}$ match those given in Eq. (3). The similarity in the parameter trends points towards the spatial correlation that exists in the ship airwake aft of the obstacle. Predictions using these updated parameter relations are shown in Figure 16, where good agreement with CGE/VorTran-M is noted.

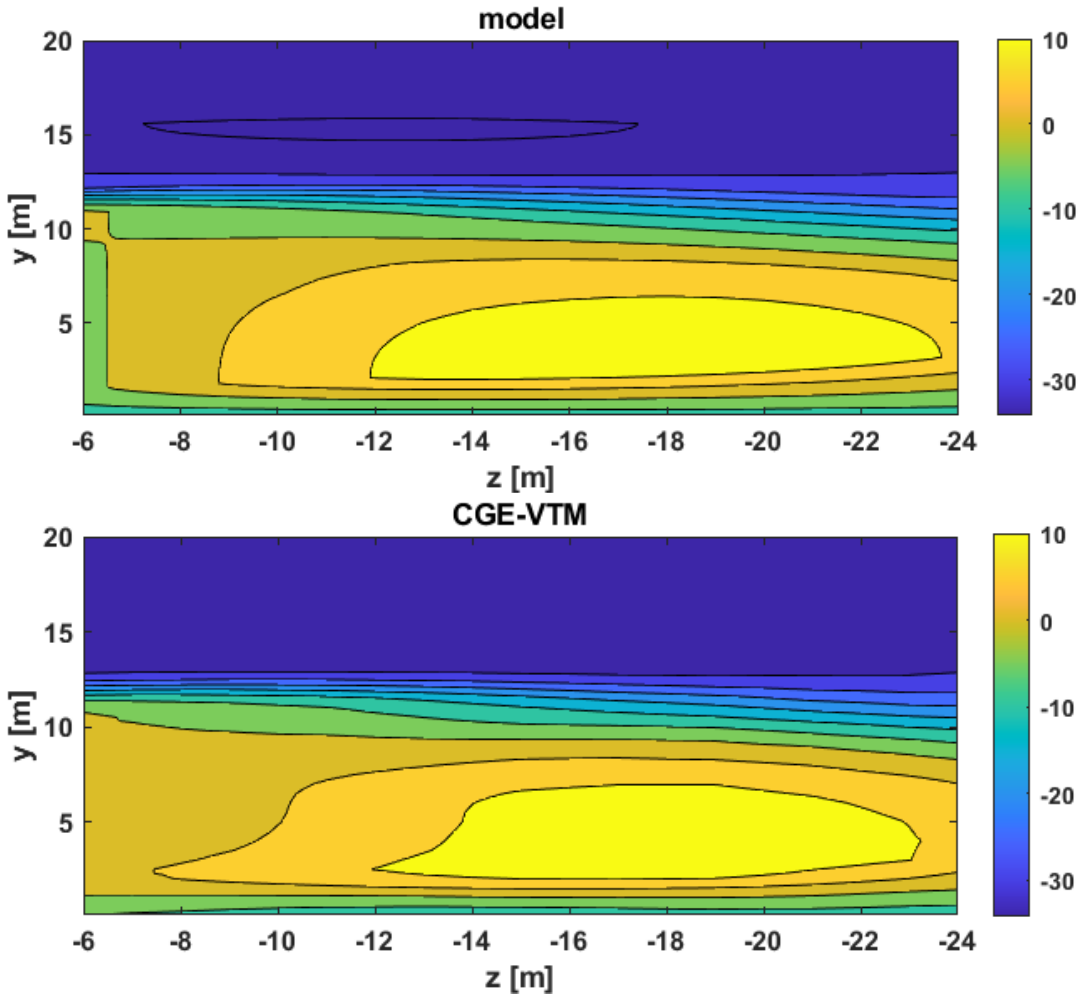

Figure 16: Contour of longitudinal velocity profile across diagonal plane obtained using model with input relations given by Eq. (4) (top) and CGE/VorTran-M (bottom).

Discussion

Using the simplified nondimensional parameter equations shown in Eqs. (3) and (4) together with the modified Banks and Meroney model, we can readily predict the time-averaged longitudinal velocity profile along the $x = 0W$, $y = 0.5H$ and diagonal planes for a given rectangular obstacle, whilst also drawing insights into flow phenomena. An approach similar to the 3D airwake reconstruction discussed in the previous progress report can be employed to reconstruct the time-averaged longitudinal velocity. This can be combined with fluctuating velocities obtained from spectral characterization using, for instance, Strouhal shedding frequencies, to obtain representative longitudinal velocity airwake data. The scalability of the model (both the modified Banks and Meroney model and nondimensional parameter relations determined here) will be tested in the subsequent progress report, where flow over rectangular configurations of varying dimensions will be considered. Extension to the vertical and lateral velocity profiles will also be considered.

Plans for the Next Reporting Period

In the next reporting period, we will build upon the understanding of the types of flowfields experienced by naval aviators described above and continue to quantify the scales and nature of the relevant primary flow structures based on the ongoing CFD predictions. Development of representative "canonical" surrogate flowfields will continue, and wwe will work on testing them out in CASTLE Example Helicopter simulations. On December 5th, we received notification that the V-22 program office has approved our OPSEC plan, and we will be able to use the CASTLE V-22 aircraft model for this project. Once CHARM has been fully integrated with CASTLE and the Example Helicopter Model, we will integrate it with the V-22 model and confirm operation.

References

1. Smith, M.J., A. Jones, A. Grubb, and J. Lefebvre. *Identification and Quantification of the Role of Turbulence in Aircraft/Ship Aerodynamics*. *ONR Annual Review*. 2020. Arlingon, VA.
2. Silva, M.J., D.A. Wachspress, D.P. Gaublomme, E.W. Hayden, T.S. Davis, and T. Fean. *The Role of Modeling & Simulation in the Mitigation of V-22 Tiltrotor Formation Flight Wake-Induced Roll-off*. *72nd Annual Forum of the American Helicopter Society*. 2016. West Palm Beach, FL.
3. Whitehouse, G.R. and R.E. Brown. *Modelling a Helicopter Rotor's Response to Encounters with Aircraft Wakes*. in *28th European Rotorcraft Forum*. 2002. Bristol, UK.
4. Whitehouse, G.R. and R.E. Brown. *Helicopter Rotor Response to Wake Encounters in Ground Effect*. in *59th Annual Forum of the American Helicopter Society*. 2003. Phoenix, AZ.
5. Whitehouse, G.R. and R.E. Brown, *Modelling the Mutual Distortions of Interacting Helicopter and Aircraft Wakes.* Journal of Aircraft, 2003. **Vol. 40**(No. 3): p. pp. 440-449.
6. Whitehouse, G.R. and R.E. Brown, *Modelling a Helicopter Rotor's Response to Wake Encounters.* The Aeronautical Journal, 2004. **Vol. 108**(No. 1079): p. pp. 15-26.
7. Whitehouse, G.R., *Helicopter Response to Vortex Encounters in the Near-Airfield Environment*, 2003, PhD Thesis, Department of Aeronautics Imperial College London.
8. ADS-33E-PRF. *Aeronautical Design Standard Performance Specification Handling Qualities Requirements for Military Rotorcraft*. in *US Army Aviation and Missile Command, Aviation Engineering Directorate*. 2000. Redstone Arsenal, Alabama.
9. Howlett, J.J., *UH-60A Black Hawk Engineering Simulation Program - Volume I - Mathematical Model*, 1981, NASA-CR-166309.
10. Keller, J.D., D.A. Wachspress, and J.C. Hoffler. *Pilot Evaluation of a Real-Time Free Wake Model in a Navy Rotorcraft Fleet Trainer*. *73rd Annual Forum of the American Helicopter Society* 2017. Fort Worth, TX.
11. Sousa, J.M.M., *Turbulent Flow Around a Surface-Mounted Obstacle Using 2D-3C DPIV.* Experiments in Fluids, 2002. **Vol. 33**(No. 6): p. pp. 854-862.
12. Keller, J.D., G.R. Whitehouse, A.H. Boschitsch, J. Nadal, J. Jeffords, and M. Quire. *Computational Fluid Dynamics for Flight Simulator Ship Airwake Modeling*. in *Interservice/Industry Training, Simulation, and Education Conference (I/ITSEC) 2007*. 2007. Orlando, FL.
13. Horn, J.F., J.D. Keller, G.R. Whitehouse, and R.M. McKillip Jr., *Analysis of Urban Airwake Effects on Heliport Operations at the Chicago Children's Memorial Hospital*,

2011, Illinois Department of Transportation http://www.dot.il.gov/aero/CMH/Analysis%20of%20Urban%20Airwake.pdf.

14. Yakhot, A., H. Liu, and N. Nikitin, *Turbulent Flow Around a Wall-Mounted Cube: A Direct Numerical Simulation.* International Journal of Heat and Fluid Flow, 2006. **Vol. 27**(No. 6): p. pp. 994-1009.
15. Klotz, L., S. Goujon-Durand, J. Rokicki, and J.E. Wesfreid, *Experimental Investigation of Flow Behind a Cube for Moderate Reynolds Numbers.* Journal of Fluid Mechanics, 2014. **Vol. 750**: p. pp. 73–98.
16. Banks, D. and R.N. Meroney, *A Model of Roof-Top Surface Pressures Produced by Conical Vortices: Model Development.* Wind and Structures, 2001. **Vol. 4**(No. 3): p. pp. 227–246.
17. Banks, D. and R.N. Meroney, *A Model of Roof-Top Surface Pressures Produced by Conical Vortices: Evaluation and Implications.* Wind and Structures, 2001. **Vol. 4**(No. 3): p. pp. 279–298.